Remote Sounding of High Clouds: I. Calculation of Visible and Infrared Optical Properties from Lidar and Radiometer Measurements

C. M. R. PLATT

CSIRO Division of Atmospheric Physics, Aspendale, Victoria, Australia

(Manuscript received 6 October 1978, in final form 16 June 1979)

ABSTRACT

This article describes a method of determining the visible and infrared properties of high ice clouds using a ground-based lidar and infrared (IR) radiometer. A method of calibrating the lidar is described. This is followed by a method for the correction of the cloud backscatter coefficients for pulse attenuation in the clouds, using an experimentally determined backscatter to extinction ratio k. The IR emissivity is then calculated by assuming a value for the ratio between the visible extinction coefficient and the IR absorption coefficient which is invariant with altitude. This ratio is altered until the computed radiance is equal to the measured cloud radiance. Errors in the calculation of the backscatter coefficient, the visible and the IR optical depths and the IR emissivity are assessed for various errors in the backscatter to extinction ratio. It is found that errors in the cloud optical depth become extremely sensitive to errors in k when the cloud visible optical depth becomes large. However, errors in the IR optical depth and IR emissivity are considerably less because they are constrained to agree with IR radiance measurements. For "typical" cirrus, having an emissivity of 0.24, and for a standard error in k of 20%, the error in the visible optical depth is 20–30%, whereas the errors in the IR optical depth and emissivity are only 1 and 2%, respectively. The effects of a variable multiple-scattering factor on the above errors appear to be small. However, the variation of this factor is not known well enough yet in high clouds to assess the errors accurately.

Other sources of error, which will be discussed in later papers of this series, include experimental errors in the measured IR radiance and errors in the determination of the calibration factor S.

1. Introduction

A program of ground-based lidar and infrared (IR) radiometer sensing of high clouds was started several years ago to investigate the optical properties of these clouds. As exemplified by the SMIC Report (1971) such data is needed for a better understanding of climate. Recently, the Joint Organizing Committee of the Global Atmospheric Research Program identified Radiation and High Clouds as one of the chief problem areas of climate. Preliminary measurements made in 1970 at Adelaide with the University lidar and a CSIRO infrared radiometer demonstrated the feasibility of the method (Platt, 1973, referred to here as P1). Similar work reported in the literature is restricted to that of Evans (1968) who made some measurements on cirrus clouds and Davis (1971) who gave an analysis of lidar cirrus profiles. Werner (1973) also reported some lidar and radiometer measurements on cirrus. Since the early measurements a high-power ruby lidar installed at Aspendale (Allen and Platt, 1977) has enabled the program of observations to continue. This article describes methods which have been developed to analyze the lidar and radiometer data and to calculate the cloud visible (short-wave) optical depth and the IR emissivity.

The importance of cloudiness as a component of climatic control has been amply demonstrated (Manabe and Wetherald, 1967; Schneider, 1972; Paltridge 1974a, b; Cess, 1976). However, the actual climatic *effects* of changes in cloud cover are not well understood. If there is a change dA_c in cloud cover, then if compensating mechanisms are disregarded, there will be a corresponding change dF_n in the net radiant flux at the top of the atmosphere. An increase, say, in cloud cover reduces the solar input through the increased albedo α_c of the clouds compared to that of the earth's surface (except in polar regions, where ice albedo can be greater than cloud albedo). But increased cloud cover also reduces the infrared output, which is an opposing process. The net radiant flux change $\partial F_n/\partial A_c$ then depends on which of the above two processes is dominant. For low clouds of the cumulus variety, the solar albedo increase is usually dominant, whereas for high clouds such as cirrus, frontal clouds or high-reaching cumulonimbus, the infrared reduction can be dominant. The global average of $\partial F_n/\partial A_c$ depends on many factors such as solar angle, ground albedo, mean cloud top and so on. Theoretical studies with simple models (Manabe and Wetherald, 1967; Schneider, 1972) have yielded an overall dominant solar albedo effect so that $\partial F_n/\partial A_c$ is negative. Cess (1976) employed zonal changes in climatological cloud

0021-8952/79/091130-14$07.50

data as a pointer to what would happen to $\partial F_n/\partial A_c$ for temporal changes in cloud amount. He concluded that global $\partial F_n/\partial A_c$ was close to zero. However, this was not true for individual zones.

Given a perturbation in cloud amount, various atmospheric mechanisms can feed back to either amplify or damp this perturbation. The origins of such feedback, let alone their sign, are not yet fully understood. Much more and better data on the optical properties of clouds is needed. Because of the multivarious nature of clouds, they are perhaps better classified by their statistical properties. In that case, many observations on many cloud systems are required. A remote recording system is ideal for this purpose.

Lidar and IR radiometer measurements of clouds give the optical properties of the clouds in different wavelength bands in the shortwave and longwave regions, respectively. The optical properties at other wavelengths in the two regions can then be deduced using known theoretical relationships. But the lidar pulse must penetrate the clouds fully and return to the receiver in order that the full cloud extent in the atmosphere can be monitored. For low clouds of the cumulus variety, the penetration is only $\sim$100 m, but for high-level ice clouds, the penetration can be $>$4 km, basically because of the low water content of ice clouds coupled with the larger particle size. High ice clouds are thus amenable to lidar observations, providing that lower cloud does not intervene.

The IR radiometer measurements yield the optical depth of the cloud at some wavelength in the atmospheric window. The inferred value is actually the absorption optical depth plus a small scattering effect ($\sim$5%) which can be calculated separately. Using the curve of the refractive index of ice versus wavelength, the IR extinction and absorption can then be computed at other wavelengths assuming that the particles are either ice spheres or ice cylinders. Then the known absorption properties of water vapor and carbon dioxide can be added so as to deduce the total IR radiative properties of the cloud.

Lidar observations when coupled with an assumed effective backscatter-to-extinction ratio yield an estimate of the cloud optical depth at a visible wavelength (0.694 μm for a ruby lidar). Now the cloud spectral albedo can be calculated theoretically for a given optical depth and wavelength (e.g., Liou, 1973). Furthermore, the refractive index of ice is relatively independent of wavelength in the shortwave part of the spectrum so that, in principle, the cloud optical depth at one wavelength can be related to the total cloud shortwave albedo for a given theoretical model. However, the theoretical calculations are hindered, at present, by the uncertainty in the shape of the scattering phase function for ice crystals. This restricts the accuracy of the calculated albedo-optical depth relationships.

Lidar observations also give the height profile of the backscatter coefficient $B(\pi,z)$ once the backscatter has been corrected for pulse attenuation. Now, if the cloud particle size distribution and type is independent of height, then $B(\pi,z)$ is proportional to liquid water content. There is evidence that in cirrus clouds, the size distribution and ice crystal habit vary only slowly with altitude (Heymsfield, 1975) so that the $B(\pi,z)$ profiles should give useful information on the height distribution of liquid water content in these clouds.

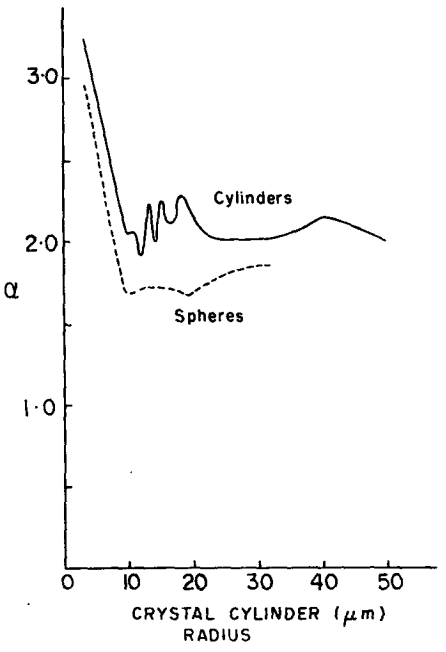

FIG. 1. The ratio α plotted against cylinder radius for both a cylinder scattering model and a Mie spherical model. In the latter case, the radius of the sphere is made equal to the equivalent spherical radius of the cylinder when its length is 4 times the radius. (The equivalent sphere has a cross-sectional area which is one-quarter the area of the cylinder.)

The basic assumptions made in the following analyses are that ratios between certain cloud optical parameters are independent of height, or position in a cloud. The first of these is k, the backscatter to extinction ratio. Now k is dependent only on the shape of the volume scattering phase function. Cirrus clouds are composed of a mixture of several types of ice crystal, namely, bullet-shaped crystals, either singly or in rosettes, hexagonal columns, with hollow cavities and irregular crystals (e.g., Heymsfield, 1975). Because of their complex structures, these crystals would be expected to act roughly like isotropic scatterers in the back hemisphere (e.g., Huffman, 1970) so that k would be fairly independent of crystal size or shape. Some support for this argument is given by the laboratory measurements of Sassen (1978), where k for complex crystal aggregates is indeed found to be independent of crystal type. A second quantity which is considered to be constant is the ratio (α) of the visible extinction coefficient to the IR absorption

coefficient. Ice crystals in cirrus generally have dimensions of 50 to 1000 μm in length and about $\frac{1}{4}$ this value in breadth. These dimensions are greater than both the wavelengths in the visible spectrum and the infrared atmospheric window so that the extinction cross sections of these particles would be close to twice the geometric cross-sectional area (twice, because of diffraction), and independent of crystal shape. Also, as ice is very absorbing, the absorption cross section of ice crystals would similarly be close to the geometric cross section. Theoretical Mie calculations of the ratio α for both spheres and long cylinders are shown in Fig. 1. Although its mean value in each case is not exactly equal to 2, α is independent of radius to within 10% for a crystal of radius (breadth) >10 μm.

Another phenomenon which is relevant is that ice crystals in the size range encountered in the atmosphere can assume preferred free-fall orientations so that some effects of viewing vertically (e.g., specular reflections, Platt *et al.*, 1978) may be evident. These effects occur generally at temperatures $\gtrsim -30$°C and they will be discussed in Part IV of this series.

The lidar and radiometer observations are made by having the lidar and radiometer close together and pointing along the same direction, thus ensuring that both instruments sample the same portion of cloud. For this reason it is necessary that the two instrument receivers have comparable angular fields of view. Simultaneous observations are made at predetermined time intervals. In order to minimize the distance to the cloud, it is most convenient to point both instruments in the vertical. This article describes how data is analyzed to give the required quantities. It forms the first of a series of papers on the optical properties of high clouds. In Part II a description of the experimental methods and measurements of cirrus emissivity will be given. Part III will provide a description of calculations of the effects of multiple-scattering in the lidar receiving beam. In Part IV, measurements and analysis of visible optical depth and cloud backscatter profiles will be provided.

2. Cloud—Visible and infrared optical quantities

The fundamental quantities that are required to describe the optical properties of clouds are the cloud visible extinction optical depth $\delta_c(h)$ and the IR emissivity ϵ. $\delta_c(h)$ is related to the volume extinction coefficient $\sigma_c(z)$ and backscatter coefficient $B(\pi,z)$ (in m^{-1}) by the equations (see Appendix for list of symbols)

$$\delta_c(h)=\int_{z_0}^{z_T}\sigma_c(z)dz, \tag{1}$$

$$B_c(\pi,z)=k\sigma_c(z), \tag{2}$$

where k is the backscatter to extinction ratio. Then

$$\delta_c(h)=\frac{1}{k}\int_{z_0}^{z_T}B_c(\pi,z)dz, \tag{3}$$

where z_0 and z_T are the cloud-base and cloud-top altitudes, respectively, and the lidar is pointing vertically.

If the effects of scattering are neglected (see Section 6) the IR emissivity is related to the absorption optical depth $\delta_A(h)$ in the same wavelength band by

$$\epsilon=\{1-\exp[-\delta_A(h)]\}. \tag{4}$$

In order to obtain $\delta_c(h)$ and ϵ, values of $B_c(\pi,z)$, k and $\delta_A(h)$ are therefore needed although, as discussed below, a less accurate value of ϵ can be obtained directly from radiance data.

The information obtainable from a single-lidar shot and a simultaneous measurement of the cloud IR radiance is first considered. The single-lidar shot gives the attenuated backscatter coefficient $B_c'(\pi,z)$ which is defined by

$$B_c'(\pi,z)=B_c(\pi,z)\exp\left[-2\int_{z_0}^{z}\sigma_c(z)dz\right], \tag{5}$$

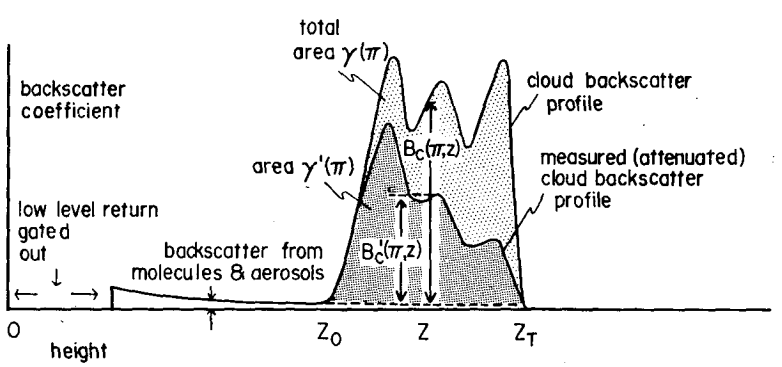

FIG. 2. Schematic of a lidar cloud return, showing the measured attentuated backscatter coefficients $B_c'(\pi,z)$, the correct backscatter coefficients $B_c(\pi,z)$, and the corresponding areas under the two curves, $\gamma'(\pi)$ and $\gamma(\pi)$, respectively.

where the term in the exponential describes the two-way attenuation of the lidar pulse as it travels from cloud base z_0 to height z and back to the base. A lidar return is shown schematically in Fig. 2 together with the "correct" backscatter profile.

An infrared emissivity can also be obtained from data taken at one single time by relating the vertical IR radiance I_c at cloud base to the IR spectral blackbody radiance $I_B(\bar{T})$ at the mid-cloud temperature $\bar{T}$. The latter is obtained from aerological data, the mid-cloud altitude being determined from the lidar cloud profile. We denote this emissivity by ϵ^* so that

$$\epsilon^* = I_c/I_B(T). \tag{6}$$

To obtain I_c, the measured IR radiance at the ground is corrected for the gaseous emittance (mainly water vapor with a small CO_2 contribution) and transmittance of the intervening atmosphere. This aspect will be considered in Part II.

Additional information is needed to correct the values of $B_c'(\pi,z)$ for pulse attenuation and this is obtainable from a series of lidar shots together with calculation of cloud IR emissivity ϵ^*. The values of $B_c'(\pi,z)$ are first integrated through each cloud profile to give the apparent integrated backscatter $\gamma'(\pi)$:

$$\gamma'(\pi) = \int_{z_0}^{z_T} \left\{ B_c(\pi,z) \exp\left[-2\int_{z_0}^{z} \sigma(z'')dz'' \right] \right\} dz. \tag{7}$$

By putting

$$B_c(\pi,z) = k\sigma_c(z), \quad \delta(z-z_0) = \int_{z_0}^{z} \sigma_c(z'')dz'',$$

and changing variables, Eq. (7) can be integrated to obtain (Platt, 1973)

$$\gamma'(\pi) = \frac{k}{2}\{1-\exp[-2\delta_c(h)]\}. \tag{8}$$

The assumption is now made that $\delta_c(h) = \alpha\delta_A(h)$. Using also Eq. (4), Eq. (8) becomes

$$\gamma'(\pi) = \frac{k}{2}\left[1-\exp\left(-2\alpha \log\frac{1}{1-\epsilon} \right) \right]. \tag{9}$$

When $\epsilon \to 1$, then $\gamma'(\pi) = k/2$, or $k = 2\gamma'(\pi)$. Thus calculation of $\gamma'(\pi)$ when the cloud is optically thick gives a value of k. Alternatively, $k/2$ can be obtained from a fit of (9) to a plot of values of $\gamma'(\pi)$ versus values of ϵ^*.

Having obtained a value of k, the values of $B_c'(\pi,z)$ can be corrected for pulse attenuation. This can be accomplished in two ways. Eq. (5) can be inverted and solved for $B_c(\pi,z)$ by an iterative procedure, as was done in Platt (1973). Alternatively, $B_c(\pi,z)$ can be solved analytically, as follows (see, e.g., Davis, 1969; Fernald *et al.*, 1972).

Consider integration of Eq. 5 from cloud base z_0 to some height z in the cloud. Then

$$\int_{z_0}^{z} B_c'(\pi,z'')dz'' = (k/2)\left\{ 1-\exp\left[-\frac{2}{k}\int_{z_0}^{z} B_c(\pi,z'')dz'' \right] \right\}. \tag{10}$$

Rearranging this equation gives

$$\exp\left[-(2/k)\int_{z_0}^{z} B_c(\pi,z'')dz'' \right] = \left[1-(2/k)\int_{z_0}^{z} B_c'(\pi,z'')dz'' \right]. \tag{11}$$

But

$$\exp\left[(-2/k)\int_{z_0}^{z} B_c(\pi,z'')dz'' \right] = B_c'(\pi,z)/B_c(\pi,z). \tag{12}$$

Therefore, from Eqs. (11) and (12),

$$B_c(\pi,z) = B_c'(\pi,z) \Big/ \left[1-(2/k)\int_{z_0}^{z} B_c'(\pi,z'')dz'' \right]. \tag{13}$$

Having solved for $B_c(\pi,z)$, a value of $\delta_c(h)$ for each lidar shot is obtained using Eq. (3).

A more accurate value of ϵ can now be calculated. The method assumes a ratio g between $\sigma_A(z)$ and the visible extinction coefficient $\sigma_c(z)$ $[=B(\pi,z)/k]$ where g is constant through one profile. This enables the IR radiance [say, $I_c(t)$] to be computed using a radiative transfer equation. Then, by varying the value of g, $I_c(t)$ can be tuned to the measured radiance value I_c. This leads to values of the IR absorption optical depth $\delta_A(h)$ (making an appropriate correction for cloud particle scattering) and thus the IR emissivity ϵ. This method requires an *a priori* value of k in order to calculate values of $B_c(\pi,z)$. Thus an initial value of k must still first be obtained from a plot of $\gamma'(\pi)$ versus ϵ^*.

A complication in the determination of the optical depth $\delta_c(h)$ is that multiple scattering (MS) of the lidar pulse by particles in the receiver beam causes more of the lidar radiation to return to the receiver aperture than otherwise would be the case. MS thus effectively reduces the experimentally measured optical depth. If the MS optical depth is $\delta_c''(z-z_0)$ between cloud base and altitude z, then an MS factor $\eta(z-z_0)$ can be defined as

$$\delta_c''(z-z_0) = \eta(z-z_0)\delta_c(z-z_0), \tag{14}$$

where $\eta(z-z_0)$ has a value less than unity and it may vary with altitude. Eqs. (5), (8) and (9) for the attenuated backscatter coefficient and the integrated

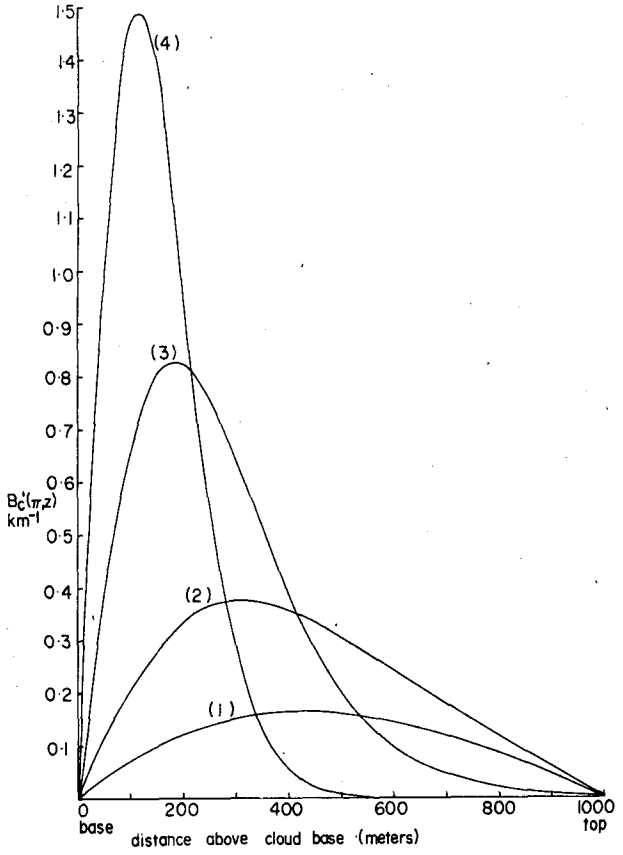

FIG. 3. Simulated lidar returns from model parabolic-shaped clouds. The backscatter coefficient $B_c(\pi,z)$ is given (for $z_0<z<z_T$) by $B_c(\pi,z)=B(\pi)_m\{1+4[(z-z_0)-(z_T-z_0)]^2/(z_T-z_0)^2\}$. In curves 1, 2, 3 and 4, values of $B(\pi)_m$ are 0.2, 0.6, 2.1 and 6 km^{-1}, respectively. η is equal to 0.5 and $k/\eta=0.6$ ($k=0.3$). Corresponding values of $\delta_c(h)$ are 0.444, 1.33, 4.67 and 13.3 and the cloud depth is 1 km. Values of IR emissivity ϵ are 0.20, 0.49, 0.90 and 0.97.

backscatter then have to be modified as

$$B'(\pi,z)=B(\pi,z)\exp[-2\eta(z-z_0)\delta_c(z-z_0)], \quad (15)$$

$$\gamma'(\pi)=[k/2\bar{\eta}(h)]\{1-\exp[-2\eta(h)\delta_c(h)]\}, \quad (16)$$

$$=[k/2\bar{\eta}(h)]\left\{1-\exp\left[-2\eta(h)\alpha\log\frac{1}{1-\epsilon}\right]\right\}, \quad (17)$$

where $\bar{\eta}(h)$ is a weighted mean of $\eta(z-z_0)$ through the cloud. Eq. (13) for the solution of $B_c(\pi,z)$ becomes

$$B_c(\pi,z)=\frac{B_c'(\pi,z)}{\left\{1-[2\bar{\eta}(h)/k]\int_{z_0}^{z}B_c'(\pi,z'')dz''\right\}}. \quad (18)$$

From Eq. (17), $k=2\bar{\eta}(h)\gamma'(\pi)$ when $\epsilon\rightarrow 1$ so that to determine $\delta_c(h)$, $\bar{\eta}(h)$ must be known.

Fig. 3 shows simulated attenuated cloud profiles for four cases, ranging from weak to very strong, pulse attenuation. In profile 4, the lidar pulse is attenuated completely before cloud top and so the area under the curve is equal to $k/2\eta(=0.3)$. The original parabolic cloud profile was chosen as reminiscent of observed profiles. These profiles will be discussed in Part III.

The following sections describe the details in the above procedures and the computational errors which arise from various errors in experimental data. The effects of multiple scattering are discussed as well as methods of optimization of the value of k from experimental data. Section 3 describes how a lidar is calibrated.

3. Calibration of the lidar

In order to determine values of the attenuated backscatter coefficient $B_c'(\pi,z)$, the return power $P(z)$ at the laser receiver must first be calibrated in terms of the backscatter coefficient and range. This is done using a target of known backscatter, which can be either a solid artificial target, or the atmosphere itself. For the latter (used in the present study) the backscatter coefficient for Rayleigh scattering and its variation with height is calculated from the atmospheric temperature and pressure profiles. Then the lidar can be calculated against a known backscatter coefficient at some range where the aerosol and cloud particle content of the atmosphere is estimated to be negligible. This criterion can be fulfilled at altitudes just above the tropopause, given certain synoptic situations (e.g., Bartusek *et al.*, 1970).

The reflected lidar pulse power $P(z)$ at the laser receiver from a range z can be written

$$P(z)=P_0(c\Delta tA/8\pi z^2)B(\pi,z)\{\exp[-2\delta(z)]\}, \quad (19)$$

where P_0 is transmitted power, c is the velocity of light, Δt is the pulse length. A is the receiver area, $B(\pi,z)$ is the backscatter coefficient and $\delta(z)$ is the total optical depth of the atmosphere at the laser wavelength between the ground and range z. If the scatter occurs within a cloud then $B(\pi,z)$ is the sum of components from molecular, aerosol and cloud particle backscatter. Thus, $B(\pi,z)=B_R(\pi,z)+B_a(\pi,z)+B_c(\pi,z)$. Similarly, $\delta(z)$ can be written $\delta_R(z)+\delta_a(z)+\delta_c(z-z_0)$.

A calibration is preferably done in an atmosphere which contains no cloud; i.e., before or after the passage of the cirrus clouds. With the present instrumentation, this causes minimum error in the results, because all the return signal voltages are normalized to the relative output energy which is read off an energy monitor. Providing that the energy monitor is stable, one calibration is sufficient for all time. However, it is preferable to check the calibration as often as is required, in order to check on any drifts in the energy monitor or the receiver optics.

If J is the transmitted energy measured on the energy monitor, and J_0 is a "standard" energy (taken as 1 J) then the return power is normalized as $P(z)$ (J_0/J), to give $P(z)$ J^{-1} of transmitted energy.

Consider first the clear-sky case where, at a level z_1, it is estimated that there is molecular scattering only but that below z_1 aerosol layers exist. If a power $P(z_1)$ is returned from level z_1, what is actually measured is a voltage $v(z_1)$, where $P(z_1)=Cv(z_1)$ and C is a system Constant. Now

$$P(z_1)z_1^2(J_0/J) = \zeta B_R(\pi,z_1)\exp\{-2[\delta_R(z_1)+\delta_a(z_1)]\} \quad (20)$$

$$= Cv(z_1)z_1^2(J_0/J_1), \quad (21)$$

where ζ is another constant. Then

$$\zeta/C = v(z_1)(J_0/J_1)z_1^2/B_R(\pi,z_1) \times\exp\{-2[\delta_R(z_1)+\delta_a(z_1)]\} = S, \quad (22)$$

where S is a calibration constant.

The terms $B_R(\pi,z_1)$ and $\delta_R(z_1)$ can be calculated from aerological data. This leaves the term $\delta_a(z_1)$. If the calibration level z_1 is near the tropopause, then $\delta_a(z_1)$ is approximately equal to the total aerosol optical depth, or atmospheric turbidity.

Now, for a different shot with a cloud present the return $P(z_2)$ from inside a cloud can be written

$$P(z_2)z_2^2(J_0/J_2) = \zeta[B_R(\pi,z_2)+B_a(\pi,z_2)+B_c(\pi,z_2)] \exp\{-2[\delta_R(z_2)+\delta_a(z_1)+\delta_c(z_2-z_0)]\} \quad (23)$$

or

$$\frac{v(z_2)z_2^2(J_0/J_2)}{S} = [B_R(\pi,z_2)+B_a(\pi,z_2)+B_c(\pi,z_2)] \times\exp\{-2[\delta_R(z_2)+\delta_a(z_2)+\delta_c(z_2-z_0)]\}. \quad (24)$$

Referring to Fig. 2, we consider the components making up the return voltage. Assuming that the background sky-radiance d.c. level has previously been subtracted, then $v(z_2)$ can be written

$$v(z_2) = v_B + v_{C'}, \quad (25)$$

where v_B is the voltage due to aerosol and molecular returns and v_C is the voltage due to cloud returns.

Then

$$\frac{v_Bz_2^2(J_0/J_2)}{S} = [B_R(\pi,z_2)+B_a(\pi,z_2)]\exp\{-2[\delta_R(z_2) +\delta_a(z_2)+\delta_c(z_2-z_0)]\}. \quad (26)$$

Subtracting Eq. (26) from (24) and simplifying gives

$$\frac{v_Cz_2^2(J_0/J_2)}{S} = B_C(\pi,z_2)\exp\{-2[\delta_R(z_2)+\delta_a(z_2) +\delta_C(z_2-z_0)]\} \quad (27)$$

$$= B_c'(\pi,z_2)\exp\{-2[\delta_R(z_2)+\delta_a(z_2)]\}. \quad (28)$$

Rearranging (28) and substituting for S from Eq. (22) gives

$$B'(\pi,z) = \frac{v_c(z_2)}{v(z_1)}\left(\frac{z_2^2}{z_1^2}\right)\frac{J_1}{J_2}B_R(\pi,z_1)\exp\{2[\delta_R(z_2)-\delta_R(z_1) +\delta_a(z_2)-\delta_a(z_1)]\}. \quad (29)$$

For cirrus clouds, most of the aerosol is below the cloud so that for a calibration close in time to the cloud measurements, $\delta_a(z_1)\approx\delta_a(z_2)$, and the exponential term in Eq. (29) is close to unity. Effects of aerosol agglomeration near the base of cirrus clouds are unknown and therefore cannot be taken into account. But they are unlikely to give more than a few percent error.

4. Calculation of correct cloud backscatter coefficient and cloud optical depth

Having obtained values of $B_c'(\pi,z)$ from a lidar calibration, the values must be corrected for pulse attenuation. As stated in Section 2, this can be accomplished either by iteration, as was done in Platt (1973) or directly, by calculating $B_c(\pi,z)$ from Eq. (18).

The analytical solution to $B_c(\pi,z)$ is obviously quicker than the iterative solution, as it only involves a single step. However, historically, the iterative solution has been used, and we use this here to investigate the errors involved in the solution for various errors in the data. It is subsequently shown that the analytical solution gives the same answers, as would be expected.

To simplify the calculations we assume that $\eta(z-z_0)$ is independent of z and we define it simply as η. Subsequently, effects of a variable $\eta(z-z_0)$ will be investigated. We define k_e as equal to k/η.

The iteration solution is obtained by inverting (15) and substituting

$$\int_{z_0}^{z} B_c(\pi,z'')dz''/k \quad \text{for} \quad \delta_c(z-z_0).$$

Then,

$$B_c(\pi,z) = B_c'(\pi,z)\exp\left[(2/k_e)\int_{z_0}^{z} B_c(\pi,z'')dz''\right]. \quad (30)$$

The cloud is divided into a number of thin layers and it is assumed that at the cloud base $B_c(\pi,z_0)=B_c'(\pi,z_0)$ and that this is true for the first layer above the base. Then $B_c(\pi,z_0)$ can be calculated at each successive layer by iteration, forming a cumulative value of the optical depth

$$\delta_c''(z-z_0)\left[=\int_{z_0}^{z} B_c(\pi,z'')dz''/k_e\right].$$

This method is similar to that of Picard (Margenau and Murphy, 1955, p. 484). Normally, only a few iterations are required at each altitude before the

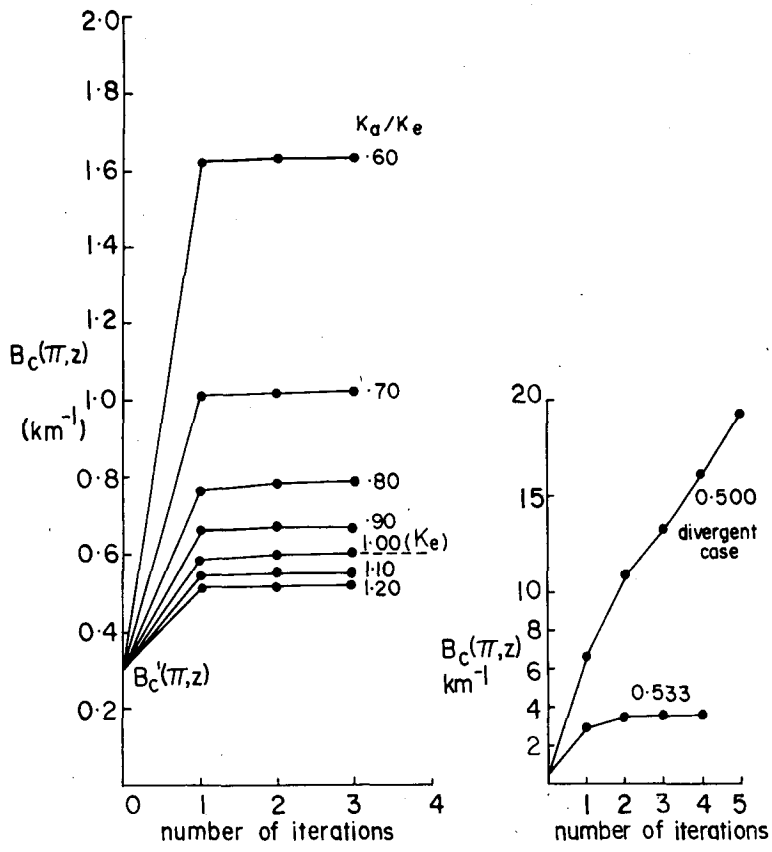

FIG. 4. Typical successive calculated values of $B_c(\pi,z)$ at one height in a cloud using the iterative method of Eq. (30). The height and backscatter coefficient corresponds to the mid-point of cloud profile 2 in Fig. 3, and also Fig. 5b, i.e., $B_c(\pi,z)=B(\pi)_m=0.6$ km^{-1}. Values of k_a/k_e are varied around unity.

solution converges—in practice, when successive values of $B_c(\pi,z)$ differ by no more than 1%.

The results of using the iteration are illustrated with the use of simulated cloud profiles similar to those of Fig. 3. The profiles of the correct backscatter coefficient are made parabolic in shape and the cloud density is characterized by a maximum backscatter coefficient $B(\pi)_m$ at cloud center. The value of the backscatter to extinction ratio is chosen as 0.3 (see P1) for each profile. The total cloud optical depth $[\delta_c(h)]$ is thus proportional to $B(\pi)_m$. The value of the MS factor η is 0.5. The simulated calculation of $B_c(\pi,z)$, starting with equivalent values of $B_c'(\pi,z)$, is performed for 50 equal intervals through the cloud depth, starting at cloud base and computing the cumulative value of $\delta_c''(z-z_0)$ and the value of $B_c(\pi,z)$ up to the cloud top. The practical application of the iteration to the real cloud case involves the inference of a single backscatter to extinction ratio k_e from experimental data. Due to errors in the data together with real fluctuations in the value of k_e, the deduced single value of k_e will not be exactly correct for any individual lidar profile. Therefore, values of k_e which are different from the "correct" value are also considered in the iterative solutions. These values of k_e are denoted k_a, and the simulations will show how values of $B_c(\pi,z)$ depart from their correct values as k_a/k_e varies.

Fig. 4 shows how the value of $B_c(\pi,z)$ converges for successive iterations at one altitude in one cloud and for various values of k_a/k_e. The curve marked k_e refers to the use of the "correct" value of $k_e=0.3/0.5$ $(=0.6)$ in Eq. (25). The successive values of $B_c(\pi,z)$ converge rapidly to the "correct" value of $B_c(\pi,z)=0.6$ km^{-1}. As k_a/k_e is reduced below unity, the calculated values of $B_c(\pi,z)$ increase rapidly until for some value of k_a, which is determined by the cloud optical depth $\delta_c(z-z_0)$, the iteration no longer converges. When k_a/k_e is increased above unity, the iteration always converges, but the final values of $B_c(\pi,z)$ are always less than the correct values. The analytical solution of Eq. (18) gives values of $B_c(\pi,z)$ which agree very closely with the final iterated values for all values of k_a. Divergence of the iteration solution corresponds to the denominator in (18) becoming zero or negative, *i.e.*,

$$2/k_a\int_{z_0}^{z} B_c'(\pi,z'')dz'' \geq 1. \qquad (31)$$

TABLE 1. Values of k_a/k_e at which divergence in the iteration of Eq. (30) first occurs, for different cloud optical depths.

$\delta_c(h)$	k_a/k_e
0.5	0.5
1.0	0.77
1.5	0.893
2.0	0.942
2.5	0.974
3.0	0.989

Figs. 5a–5c illustrate the calculated values of $B_c(\pi,z)$ at each of the 50 intervals in the cloud and for three different values of $B(\pi)_m$. In Figs. 5a and 5b the calculated values of $B_c(\pi,z)$, when $k_a/k_e=1$, are coincident to better than 0.1% with the original values. In Fig. 5c, a small error is introduced by the use of only 50 finite intervals. In Figs. 5a and 5b, the iteration converges at every point to cloud top for the values of k_a/k_e shown. In Fig. 5c, one curve is shown where the iteration no longer converges at 600 m above cloud base. Table 1 shows the values of k_a/k_e at which the solution just converges *at cloud top* for different values of total cloud optical depth $\delta_c(h)$.

The errors introduced into the total cloud optical depth $[\delta_c''(h)=\eta\delta_c(h)]$

$$\delta_c''(h)\left[=(1/k_e)\int_{z_0}^{z_T} B_c(\pi,z)dz\right]$$

by the use of values of k_a different to k_e are summarized in Fig. 6 for four different cloud optical depths. The error in $\delta_c''(h)$ is enhanced by the fact that the integrated backscatter must be divided by k_a to derive optical depth. If $k_a \neq k_e$, an error is made in deriving $B_c(\pi,z)$ and an *additional* error is made in converting integrated backscatter $\gamma(\pi)$ into optical depth $\delta_c''(h)[=\gamma(\pi)/k_a]$. Unfortunately, the two errors are of the same sign. Thus the error in $\delta_c''(h)$ is nearly double the error in the integrated backscatter $\gamma(\pi)$. In Fig. 5c it is seen

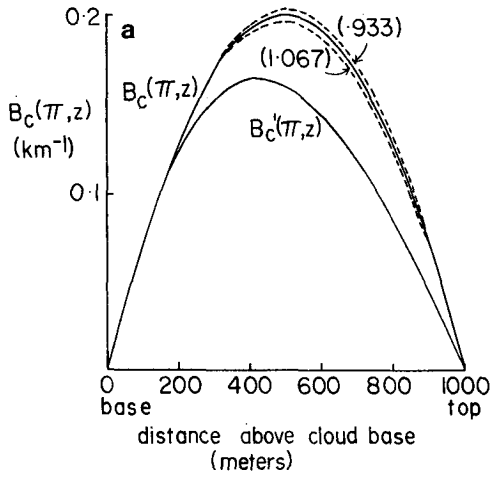

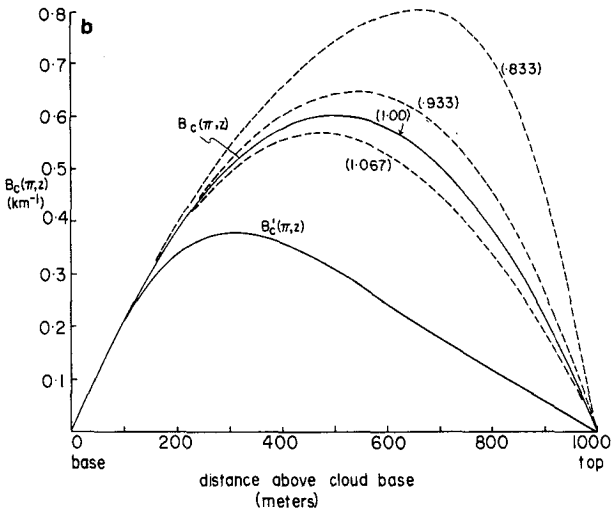

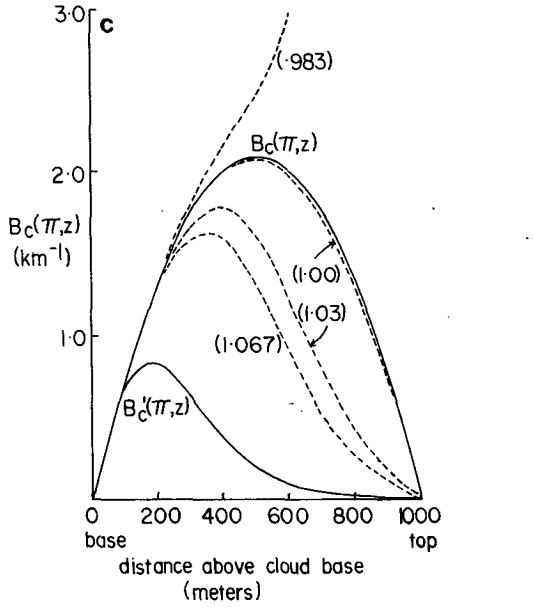

FIG. 5. (a) Calculated values of $B_c(\pi,z)$ and their variation with altitude using the same optical parameters as in curve 1, Fig. 3, and for several values of k_a/k_e. Also shown is the attenuated profile $B_c'(\pi,z)$. (b) As in Fig. 5a except with the optical parameters of curve 2, Fig. 3. (c) As in Fig. 5a but with the optical parameters of curve 3, Fig. 3.

that errors in $\delta_c''(h)$ become extremely sensitive to the difference between k_a/k_e and unity. This makes it difficult to recover the cloud optical depths correctly when they are large. However, typical cirrus emissivities are known to vary in the range from 0 to 0.5 (Pl), so that provided that k_a/k_e is less than 10 or 20% different from unity, a reasonable value of the optical depth can be found. Previous studies on cirrus (Pl) indicate that the standard error in the determination of k_e would be about ±20%. The mean IR emissivity in Pl was 0.245. Fig. 6 indicates that for this sort of emissivity the errors in the values of optical depth for

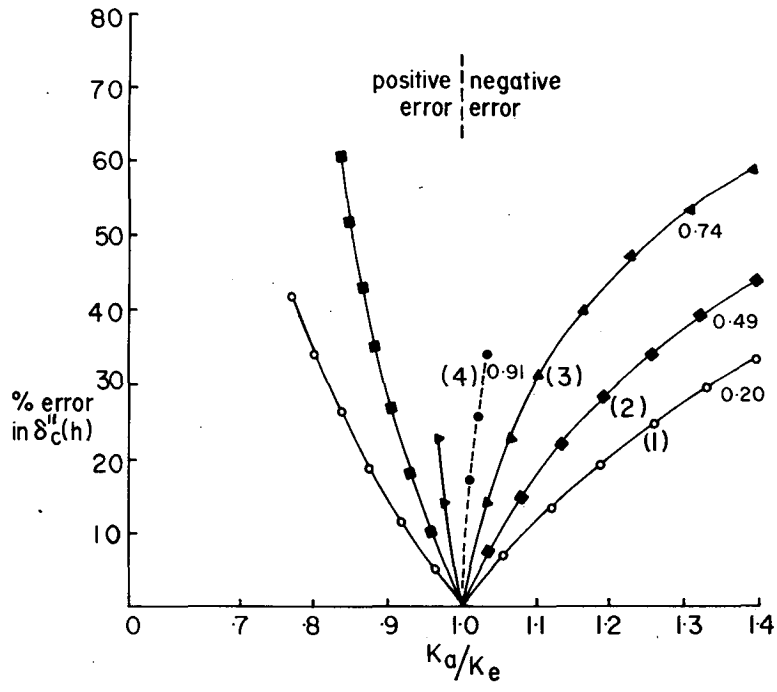

FIG. 6. Percentage error incurred in the calculation of $\delta_c''(h)$ plotted against the ratio k_a/k_e. For curves 1, 2, 3 and 4, $\delta_c(h)$ is 0.444, 1,33, 2.67 and 4.89, respectively. Corresponding values of ϵ are shown next to the curves.

single cloud profiles and for the above standard error, would be in the region of 20–30%.

The effect on the accuracy of the iterative calculation of using different number of cloud intervals is shown in Table 2 for different cloud optical depths. It is apparent that errors due to the use of finite intervals can be kept below 1% if $\Delta\delta_c(h) \lesssim 0.06$. Similar simulations to those shown in Fig. 6, but using the analytic solution of Eq. (13), and the same number of cloud intervals, are found to give values for the errors in $\delta_c(h)$ which agree to within 1% with those calculated from the iterative solution.

TABLE 2. Percentage error in cloud optical depth $\delta_c(h)$ (when $k_a/k_e=1$) for two values (N) of the total number of intervals used in the iteration calculation. Also shown is the corresponding step value of $\Delta\delta_c(h)$ for one interval.

	N			
	50	100	50	100
$\delta_c(h)$	% Error	% Error	$\Delta\delta_c(h)$	$\Delta\delta_c(h)$
0.44	0.17	0.05	0.009	0.004
0.89	0.18	0.05	0.018	0.009
1.33	0.20	0.06	0.027	0.013
1.78	0.23	0.06	0.037	0.018
2.22	0.28	0.07	0.044	0.022
2.67	0.34	0.09	0.053	0.027
3.56	0.58	0.15	0.071	0.036
4.00	0.78	0.20	0.080	0.040
4.89	1.52	0.40	0.100	0.059
5.78	3.06	0.85	0.116	0.058
6.67	6.00	1.25	0.133	0.067

The above discussion shows the types of errors inherent in the solution of $B_c(\pi,z)$. The practical application of the method to real cloud data will be discussed in Parts II and IV of this series. The simulation of equivalent errors in the IR optical depth $\delta_A(h)$ and emissivity ϵ are considered in Section 7.

5. Effects of a variable multiple-scattering factor

If the MS factor $\eta(z-z_0)$ does vary through the cloud, and allowance for this is not made in the recovery of the $B_c(\pi,z)$ profile, then a distortion of the profile will result. The value of k_a which is determined from experimental data is obtained from a plot of $\gamma'(\pi)$ versus emissivity. For a variable η, the value of $\gamma'(\pi)$ when $\epsilon \to 1$ is equal to $k/2\bar{\eta}(h)$, $\bar{\eta}(h)$ being an effective average. Use of a value of $k_e=k/\bar{\eta}(h)$ instead of $k_e=k/\eta(z-z_0)$ at a given altitude z will thus result in a distortion of the $B_c(\pi,z)$ curve. There is little information about the behavior of $\eta(z-z_0)$. The results of Kunkel and Weinman (1976) indicate that $\eta(z-z_0)$ increases from the cloud base upward and then levels off. A more detailed discussion of this behavior will be given in Part III of this series, where calculations of lidar multiple-scattering effects in cirrus clouds will be presented. A curve similar to those obtained by Kunkel and Weinman is shown in Fig. 7. $\eta(z-z_0)$ is plotted

against $\delta(z-z_0)$, the optical depth from the cloud base to altitude z. In the absence of any other information, this curve is used to simulate the effects of a variable $\eta(z-z_0)$. The expression for the curve is

$$\eta[\delta_c(z-z_0)]=0.5\{1-\exp[-2\delta_c(z-z_0)+\delta_0]\}. \quad (32)$$

For $\eta(0)=0.2$, $\delta_0=0.51$.

A simulation with the parabolic function used in Figs. 3 and 5 shows that the integrated backscatter $\gamma'(\pi)$ is now equal to 0.32 ($\epsilon \rightarrow 1$). Hence the correct value of k_e (say, k_f) to use in the recovery would now be 0.64 [i.e., $k/\bar{\eta}(h)=0.64$ and therefore $\bar{\eta}(h)=0.467$]. A simulation of errors in $\delta_c''(h)$ for various values of k_a/k_f is shown in Fig. 8. Values of $B_c'(\pi,z)$ were first calculated using $\eta(z-z_0)$ as given by Eq. (32). Values of $B_c(\pi,z)$ were then recalculated using $k_e=0.64$. The errors in $\delta_c''(h)$ are very similar to the case when η is constant (i.e., Fig. 6). Thus, despite the variation in η, the use of $k/2\bar{\eta}(h)=0.32$, as obtained from a plot of $\gamma'(\pi)$ versus ϵ, will give similar errors in $\delta_A(h)$, $\delta_c''(h)$ and ϵ to when η is constant. As before, however, the requirements for an accurate value of $k_e(k_f)$ are stringent. Also, of course, the calculated profile of $B_c(\pi,z)$ will be distorted.

6. Infrared optical depth and emissivity

A more accurate method of calculating the IR emissivity is now considered. The values so obtained will be denoted by ϵ to distinguish them from the emissivity ϵ^* (emissivity from the mid-cloud temperature). The method requires a knowledge of the true cloud backscatter profile, which thus has to be calculated first. This, in turn, requires a value for k_e (or k_a) so that it is first necessary to calculate values of ϵ^* and to plot $\gamma'(\pi)$ versus ϵ^*. Methods of optimizing the value of k_a are considered in Section 7.

The method compares experimentally measured values of downward vertical cloud radiance I_c at the cloud base with corresponding theoretical values of radiance calculated using a radiative transfer equation and an assumed ratio g between the IR absorption coefficient and the lidar effective extinction coefficient $B_c(\pi,z)/k_e$. (Values of I_c are previously corrected for atmospheric emission and transmittance below the cloud and for upwelling earth radiance which is reflected downward from the cloud. This procedure will be described in Part II.) The ratio g is tuned to bring the experimental and theoretical radiances into agreement. If $I_c(t)$ denotes the theoretical radiance, then

$$I_c(t)=\int_{z_0}^{z_T}\sigma_I(z)[I_B(z)(1-\tilde{\omega}_0)+\tilde{\omega}_0 I^s(z)] \times\left\{\exp\left[-\int_{z_0}^{z}\sigma_I(z'')dz''\right]dz\right\}. \quad (33)$$

The term $I^s(z)$ is the vertical downward radiance from cloud radiation scattered into the beam at z, $I_B(z)$ is the blackbody radiance and $\tilde{\omega}_0$ is the single scattering albedo. $I^s(z)$ can be written

$$I^s(z)=2\pi\int_0^{\pi}P(\theta)I_c(\theta)\sin\theta d\theta, \quad (34)$$

where $P(\theta)$ is the normalized scattering phase function, $I_c(\theta)$ is the cloud radiance at θ, and 2π arises from the (isotropic) azimuthal integration. Although $\tilde{\omega}$ can be appreciable the scattering phase function at window wavelengths for typical cirrus crystals is forward peaked. As a result, the scattering contribution to the radiance $I^s(z)$ is not very different from $I_B(z)$. It is thus convenient to separate the scattering and absorption contributions and write

$$I_c(t)=\int_{z_0}^{z_T}\sigma_A(z)I_B(z) \times\left[\exp-\int_{z_0}^{z}\sigma_A(z'')dz''\right]dz+I^s(c), \quad (35)$$

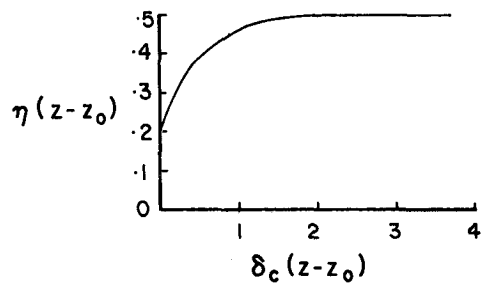

FIG. 7. Multiple scattering model variation of $\eta(z)$ plotted against value of $\delta_c(h)$ from cloud base z_0 to altitude z.

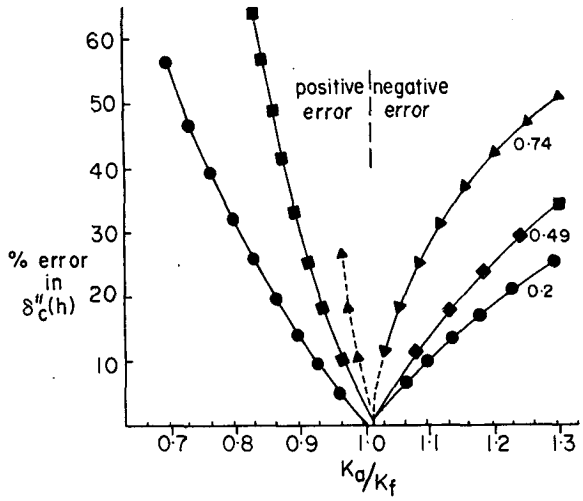

FIG. 8. Percentage errors incurred in the calculation of $\delta_c''(h)$ plotted against k_a/k_f when $\eta(z-z_0)$ varies as in Fig. 7. k_f is the effective "correct" backscatter to extinction ratio and is equal to 0.32. Optical parameters for the curves are the same as for Fig. 6. Values of emissivity are shown next to the curves.

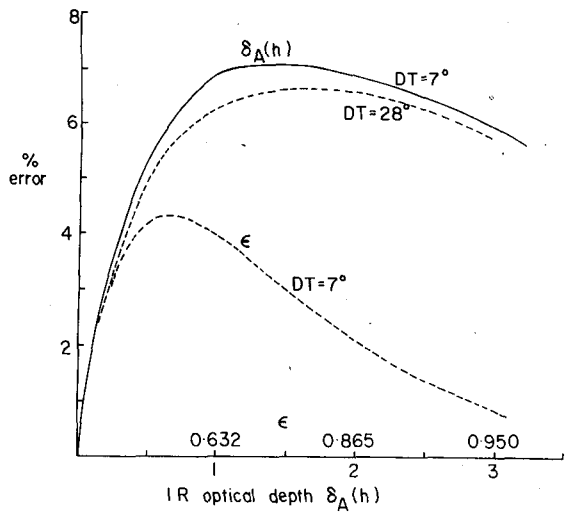

FIG. 9. Percentage errors in ϵ and $\delta_A(h)$ plotted against $\delta_A(h)$ when the contribution of scattering to the IR cloud radiance is neglected. DT represents the temperature difference between cloud base and cloud top.

where $I^s(c)$ is a correction for scattering which depends both on $\delta_A(h)$ and the temperature difference between the cloud base and the cloud top.

In practice, $\delta_A(h)$ and ϵ are computed as follows:

1) Put $\sigma_A(z)=g(B_c(\pi,z)/k_a)$, where it is assumed that η is independent of z and g is an adjustable quantity. It is evident that $g=1/\eta\alpha$.

2) Compute $I_c(t)$ by a suitable numerical integration of the first term of Eq. (35). Values of $I_B(z)$ are found from aerological temperature data and a theoretical curve relating spectral radiance I_B to temperature. Assume initially that $I^s(c)$ is negligible.

3) Vary g (making the same change in g at every altitude) until the difference $[I_c(t)-I_c]/I_c$ is less than a specified fraction (0.001 is satisfactory).

4) Compute a value of $\delta_A(h)$; then calculate ϵ from Eq. (4).

5) The correction to $I_c(t)$ for the second term in Eq. (35) is introduced as a correction to $\delta_A(h)$ and ϵ. Fig. 9 shows the errors in $\delta_A(h)$ and ϵ if scattering is neglected. These errors were estimated using a phase function appropriate to ice cylinders of 30 μm radius and 120 μm length and a wavelength of 11 μm (G. L. Stephens, private communication). The scattering radiance $I^s(z)$ was calculated by a numerical method using 20 angles (θ) between 0 and $\pi/2$. The angles were chosen to represent equal scattering probability increments from the forward direction. Only single scattering was considered. The angular cloud radiance $I_c(\theta)$ was thus assumed to be due to emission only. The contribution to $I^s(z)$ for θ between $\pi/2$ and π is only a few percent and was neglected.

As values of $\delta_A(h)$ and ϵ depend on the height profile of $\sigma_A(z)$ [i.e., $B_c(\pi,z)$], any distortion in this profile due to errors in the value of k_a will cause errors in ϵ and $\delta_A(h)$. Errors incurred in $\delta_A(h)$ for different values of k_a/k_e are shown in Fig. 10 for the same profiles of $B_c(\pi,z)$ as used in Figs. 6 and 8. Fig. 11 shows the error dependence on ϵ for two values of k_a/k_e. Also shown are the errors incurred from the use of the simple formula of Eq. 6. It is evident that fractional errors in $\delta_A(h)$ are much less than the equivalent errors in $\delta_c(h)$. The chief reason for this is that distortions in the profile of $B_c(\pi,z)$ with height due to $k_a \neq k_e$ are compensated for by variation of g. That is, the theoretical radiance $I_c(t)$ is forced by varying g to agree with I_c. Thus, if $B_c(\pi,z)$ values are too low because $k_a > k_e$ then g will be accordingly increased to compensate, and $\delta_A(h)$ will be forced toward that value *which gives a correct* $I_c(t)$. For the same reason, the absolute calibration of the lidar values of $B(\pi,z)$ is not important to the calculation of $\delta_A(h)$ as long as the relative values of $B_c(\pi,z)$ are reasonable.

Fig. 11 shows that the errors in ϵ are quite small and that they are significantly smaller than the errors in ϵ^*.

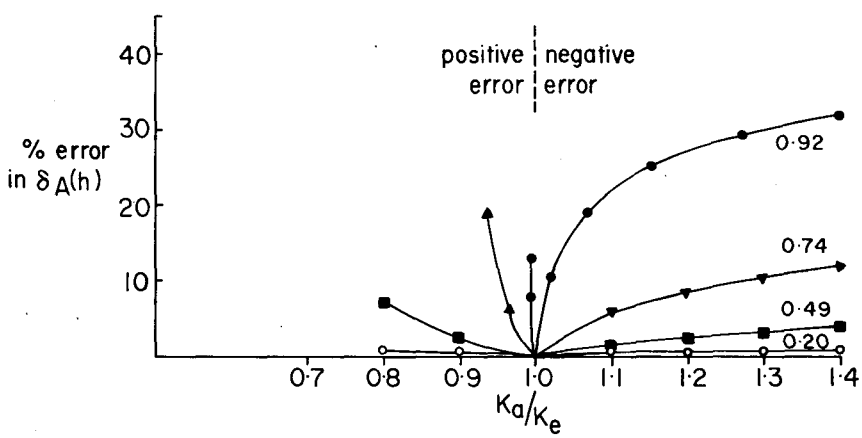

FIG. 10. Percentage errors incurred in the calculation of $\delta_A(h)$ plotted against k_a/k_e. Optical parameters for the curves are the same as for Fig. 6.

7. Optimization of the backscatter to extinction ratio

As stressed in Sections 4 and 6, errors in $\delta_c(h)$, $\delta_A(h)$ and ϵ can to some extent be minimized by determining k_a as accurately as possible, i.e., the difference between k_a and the correct value k_e must be minimized. A method of optimizing k_a has been developed as follows:

(i) Plot values of $\gamma'(\pi)$ versus values of mid-cloud emissivity ϵ^*. Fit a curve of Eq. (17) to the data and determine an initial value of k_a.

(ii) Using the above value of k_a, calculate values of ϵ by the methods of Section 6 and replot values of $\gamma'(\pi)$ versus ϵ. Determine a new value of k_a. As ϵ is generally more accurate than ϵ^*, an improved value of k_a will result.

(iii) Vary the value of k_a about the above value and recalculate values of ϵ (and g) for each value of k_a. Plot the *ratio* g against ϵ for each value of k_a. The value of k_a which makes the ratio g *independent of* ϵ is then the correct value. This is illustrated in Fig. 12, where $g/2$ is plotted against ϵ for simulated cloud profiles. If $k_a/k_e \neq 1$, then the calculated profiles of $B_c(\pi,z)$ will be distorted, resulting in a (false) dependence of the ratio g on ϵ. [We recall that in the calculation of ϵ, g is varied so to make the computed radiance $I_c(t)$ equal to the measured radiance I_c.]

This method is equivalent to that used in PI where the correlation between values of the corrected back-

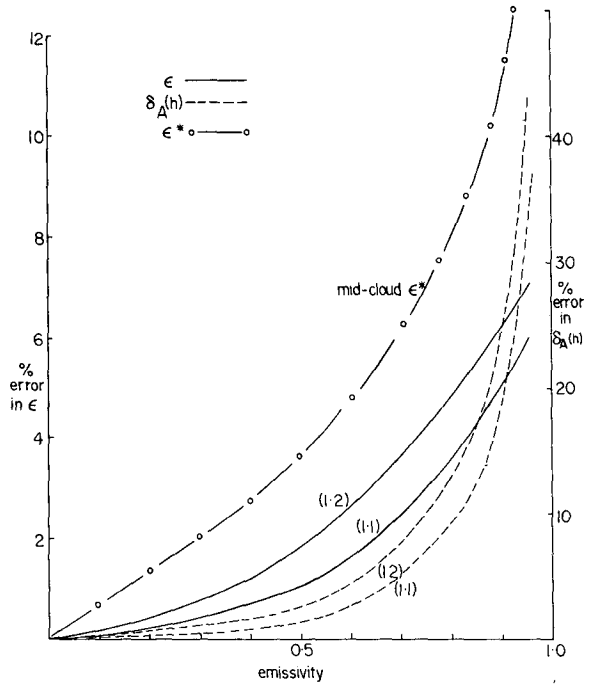

FIG. 11. Percentage errors in ϵ and $\delta_A(h)$ plotted against emissivity for two values of k_a/k_e. Also shown are the percentage errors in the mid-cloud emissivity ϵ^* which is calculated from the mid-cloud temperature $\bar{T}$ [Eq. (6)].

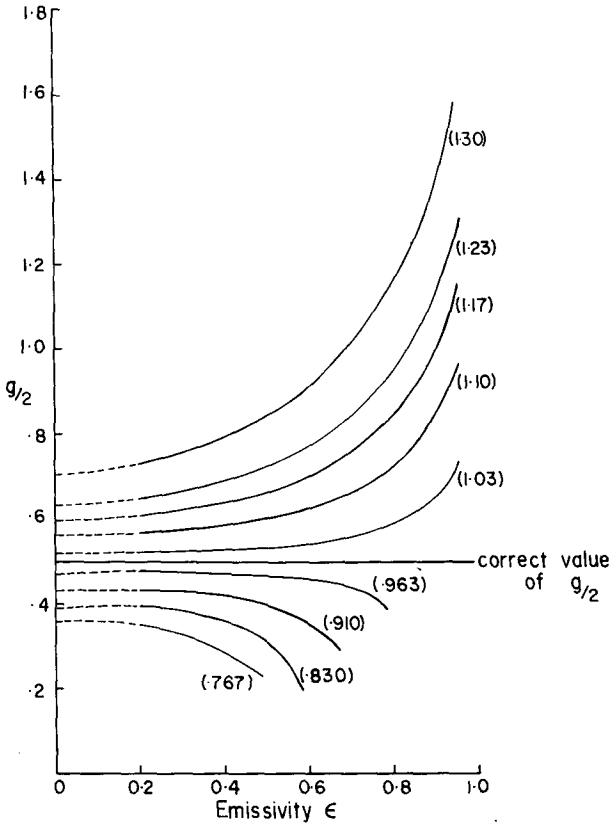

FIG. 12. Values of $g/2$ plotted against ϵ for various values of k_a/k_e (in parentheses). $g/2=0.5$ is the correct value.

scatter $\gamma(\pi)$ and the IR optical thickness $\delta_A(h)$ was maximized. The method was successful for the cloud systems treated in PI.

For any set of data, short cuts in the above procedures may be possible. For instance, a fit by eye of a plot of $\gamma'(\pi)$ versus ϵ^* may give a sufficiently accurate initial value of k_a. Similarly, for experimental data with a small scatter, step (ii) could be omitted. The general success of the whole method depends on the quality of the data and the homogeneity of the clouds.

A bonus from the above method is the determination of the ratio g. This ratio can be compared with values from theoretical models. For instance, Fig. 1 shows values of $\alpha(=1/\eta g)$ plotted against the clouds particle size, for two different models.

The curves of $g/2$ in Fig. 12 have been obtained using a value of the MS factor $\eta(z-z_0)$ which does not vary with optical depth (or altitude). However, if $\eta(z-z_0)$ does vary with optical depth and this is not taken into account in the calculation of $B_c(\pi,z)$, then the values of $B_c(\pi,z)$, and therefore of g, will be incorrect, particularly at low values of $\delta(z-z_0)$. This aspect will be considered in Part IV, when the recovery of the optical depth will be discussed in more detail.

8. Discussion and conclusion

The foregoing analysis demonstrates the feasibility of determining the IR optical depth of cirrus clouds at some wavelength in the atmospheric window and the visible optical depth at a lidar wavelength. However, the accuracy of the method is dependent on both the accuracy of the value of the experimental backscatter-to-extinction ratio and also on the optical depth of the cloud itself. At high cloud optical depths, the accuracy becomes extremely sensitive to the accuracy of the backscatter to extinction ratio which is used in the computation. However, corresponding errors in $\delta_A(h)$ and ϵ are much less. As stated before, for the average emissivity measured in Pl ($\epsilon^*=0.245$), the error in a single-cloud optical depth is estimated to be 20–30%. The corresponding errors in ϵ and $\delta_A(h)$ are 1 and 2%, respectively.

Experimental errors in the radiance, atmospheric transmittance, etc. which are not considered here will amplify the errors in $\delta_A(h)$ and ϵ and these are discussed further in Part II. Similarly errors in the calibration constant S, etc., will increase those in $\delta_c(h)$. Another large uncertainty in the final $\delta_c(h)$ values is in the value of η. In Pl, this was determined to about $\pm 30\%$ accuracy. Also, the variation of $\eta(z-z_0)$ with altitude is not well understood and more study is needed. These latter errors will be discussed in later papers which will comprise Parts III and IV of this series.

The analysis is being used at present on data obtained at Aspendale using the new lidar and radiometer system. The accuracy of future optical depth determinations will depend on the quality of data obtained. Any actual real changes in k_e for instance, can be detected as systematic departures of points from a $\gamma'(\pi)$ versus ϵ plot for one part of a cloud system, and such changes have been actually observed. Further, it has also been found that the scatter in a $\gamma'(\pi)$ versus ϵ plot is greater for cirrostratus clouds than it is for higher cirrus clouds. The errors in the optical depth measurements will thus vary from one system to the next. Emissivity calculations on large cirrostratus systems will be reported in Part II of this series.

The depolarization ratio Δ (Platt, 1977) is one guide to the homogeneity of cloud particle populations. Δ varies from ~ 0.4 for typical high cirrus clouds down to ~ 0.03 for water clouds. Mid-level clouds exhibit large variations in Δ, as might be expected (Platt, 1977; Pal and Carswell, 1977). Values of Δ are now being measured on a routine basis and they will be compared with the deduced values of k_a, η, etc.

Also, in progress is an experimental and theoretical study of the magnitude and possible variations of η in cirrus clouds. It is hoped that results from this study will improve the quality of the visible optical depth data. At present, it is possibly more accurate, at least for the higher optical depths, to calculate $\delta_c(h)$ from values of $\delta_A(h)$ and the theoretical value of α than to obtain $\delta_c(h)$ from the backscatter profiles, but with improvement in determination of η the position may be reversed and it may then be possible to detect actual variations in α. Some calculations of η using a Monte Carlo method will be presented in Part III of this series.

Acknowledgments. The author would like to thank Dr. G. T. McNice, ERL/NOAA, Boulder, Colorado, for a valuable discussion regarding the analytical solution to the lidar backscatter coefficient.

APPENDIX

List of Symbols

Visible

$\sigma_c(z)$	volume extinction coefficient of cloud particles
$\delta_c(h)$	total vertical optical depth of cloud of thickness h $[=z_T-z_0]$
$\delta_c(z-z_0)$	optical depth from cloud base z_0 to altitude z
$\delta_c''(z-z_0)$	effective optical depth with multiple scattering
$B_c'(\pi,z)$	attenuated cloud backscatter coefficient (per 4π sr m^{-1}) at altitude z
$B_c(\pi,z)$	correct cloud backscatter coefficient (per 4π sr m^{-1}) at altitude z
$\gamma'(\pi)$	integrated backscatter
$\gamma(\pi)$	correct integrated backscatter
α	$\sigma_c(z)/\sigma_A(z)=\delta_c(h)/\delta_A(h)$
η	multiple-scattering (MS) factor when assumed constant with z
$\eta(z-z_0)$	MS factor from cloud base to height z, variable with z
$\bar{\eta}(h)$	mean MS factor for cloud, when MS factor varies as $\eta(z-z_0)$
k	backscatter to extinction ratio $[=B(\pi,z)/\sigma_c(z)]$
k_e	k/η
k_a	experimental value of k_e (or k_f)
k_f	$k/\bar{\eta}(h)$
g	$1/\eta\alpha$
S	lidar calibration factor
$\delta_R(z)$	molecular extinction optical depth from surface to z
$\delta_a(z)$	aerosol extinction optical depth from surface to z
$B_R(\pi,z)$	molecular (Rayleigh) backscatter coefficient at altitude z
$B_a(\pi,z)$	aerosol (Rayleigh) backscatter coefficient at altitude z

Infrared

$\sigma_I(z)$	volume extinction coefficient $[=\sigma_A(z)+\sigma_{sc}(z)]$
$\sigma_A(z)$	volume absorption coefficient
$\sigma_{sc}(z)$	volume scattering coefficient

$\delta_I(h)$	extinction optical depth of cloud of thickness h
$\delta_A(h)$	absorption optical depth of cloud of thickness h
$\tilde{\omega}_0$	single scattering albedo $[=\sigma_{sc}(z)/\sigma_I(z)]$
ϵ	IR absorption emissivity
ϵ^*	IR absorption emissivity calculated from mid-cloud temperature $\bar{T}$
I_c	measured vertical downward radiance at cloud base
$I_c(t)$	theoretically calculated downward radiance at cloud base.

Note that the symbol for optical depth is now δ, as compared to Platt (1973) when τ was used. The change was made to agree with the new recommendations of the Radiation Commission, IAMAP (1978).

REFERENCES

Allen, R. J., and C. M. R. Platt, 1977: Lidar for multiple backscattering and depolarization observations. *Appl. Opt.*, **16**, 3193–3199.

Bartusek, K., D. J. Gambling and W. G. Elford, 1970: Stratospheric aerosol measurements by optical radar. *J. Atmos. Terr. Phys.*, **32**, 1535–1544.

Cess, R. D., 1976: Climate change: An appraisal of atmospheric feedback mechanisms employing zonal climatology. *J. Atmos. Sci.*, **33**, 1831–1843.

Davis, P. A., 1969: The analysis of lidar signatures of cirrus clouds. *Appl. Opt.*, **8**, 2099–2102.

——, 1971: Applications of an airborne ruby lidar during a BOMEX program of cirrus observations. *J. Appl. Meteor.*, **10**, 1314–1323.

Evans, W. E., 1968: Remote probing of high cloud cover via satelliteborne lidar. Final Rep. Contract NAS-49(27), NASA, Washington, DC.

Fernald, F. G., B. M. Herman and J. A. Reagan, 1972: Determination of aerosol height distributions by lidar. *J. Appl. Meteor.*, **11**, 482–489.

Heymsfield, A. J., 1975: Cirrus uncirrus generating cells and the evolution of cirriform clouds. Part I: Aircraft observations of the growth of the ice phase. *J. Atmos. Sci.*, **32**, 799–808.

Huffman, P., 1970: Polarization of light scattered by ice crystals. *J. Atmos. Sci.*, **27**, 1207–1208.

Kunkel, K. E., and J. A. Weinman, 1976: Monte Carlo analysis of multiply scattered lidar returns. *J. Atmos. Sci.*, **33**, 1772–1781.

Liou, Kuo-Nan, 1973: Transfer of solar irradiance through cirrus cloud layers. *J. Geophys. Res.*, **9**, 1409–1418.

Manabe, S., and R. T. Wetherald, 1967: Thermal equilibrium of the atmosphere with a given distribution of relative humidity. *J. Atmos. Sci.*, **24**, 241–259.

Margenau, H., and G. M. Murphy, 1955: *The Mathematics of Physics and Chemistry*, 2nd ed., D. Van Nostrand Co. Inc., 604 pp.

Pal, S. R., and A. I. Carswell, 1977: The polarization characteristics of lidar scattering from snow and ice crystals in the atmosphere. *J. Appl. Meteor.*, **16**, 70–80.

Paltridge, G. W., 1974a: Atmospheric radiation and the gross character of stratiform cloud. *J. Atmos. Sci.*, **31**, 244–250.

——, 1974b: Global cloud cover and earth surface temperature. *J. Atmos. Sci.*, **31**, 1571–1576.

Platt, C. M. R., 1973: Lidar and radiometric observations of cirrus clouds. *J. Atmos. Sci.*, **30**, 1191–1204.

——, 1977: Lidar observations of a mixed-phase altostratus cloud. *J. Appl. Meteor.*, **16**, 339–345.

——, N. L. Abshire, and G. T. McNice, 1978: Some microphysical properties of an ice cloud from lidar observation of horizontally-oriented crystals. *J. Appl. Meteor.*, **17**, 1220–1224.

Radiation Commission, International Association of Meteorology and Atmospheric Physics (IAMAP), 1978: Terminology and units of radiation quantities and measurements, E. Raschke, Ed. Boulder, Colorado, 17 pp.

Sassen, K., 1978: Backscattering cross-sections for hydrometeors: Measurements at 6328 Å. *Appl. Opt.*, **18**, 804–806.

SMIC Report, 1971: *Study of Man's Impact on Climate.* The MIT Press, 308 pp.

Schneider, S. H., 1972: Cloudiness as a global climatic feedback mechanism: The effects on the radiation balance and surface temperature of variations in cloudiness. *J. Atmos. Sci.*, **29**, 1413–1422.

Werner, C., 1973: Automatic cloud cover indicator system. *J. Appl. Meteor.*, **12**, 1394–1400.